Synergy of Wind Energy Harvesting and Synchronized Switch Harvesting Interface Circuit

Liya Zhao, Lihua Tang, Junrui Liang, *Member, IEEE*, and Yaowen Yang

***Abstract*—Due to the complex aero-electro-mechanical coupling involved in wind energy harvesting systems, power enhancing efforts in the literature are mostly devoted to structural modifications while the interface circuit is simplified to a resistive ac load. Yet the ac outputs are not applicable for practical usage. In this paper, we study the dynamics and dc power generation of galloping energy harvester. In particular, the enhancement of wind power extraction using the synchronized switching harvesting on inductor (SSHI) power conditioning circuit is emphasized. Analytical solution of the steady-state mechanical and electrical responses with the SSHI interface is derived explicitly and validated with wind tunnel experiment and circuit simulation. The performance of SSHI interface is compared to that of a standard bridge rectifier interface circuit. It shows that the SSHI interface achieves tremendous power enhancement in a weak-coupling system, and higher wind speeds render more significant power enhancement. Moreover, given the same wind condition and output power requirement, a system connected to the SSHI uses much less piezoelectric material compared to that connected to the standard circuit. With a weak-coupling harvester operating at a wind speed of 7 m/s, the SSHI can harvest up to 143% more wind power than the standard circuit.**

***Index Terms*—Aeroelasticity, galloping, piezoelectric, switching harvesting on inductor (SSHI) interface, wind energy harvesting.**

I. Introduction

RECENTLY, growing research attention has been paid to wind energy harvesting with an ultimate goal of implementing self-powered wireless sensor networks (WSNs). Some reported wind energy harvesters have taken forms of the traditional windmills via direct mechanical impact [1] or nonimpact magnetic interactions [2]. Other researchers resort to the aeroelastic instability phenomena including vortex-induced vibration (VIV) of a circular cylinder under Kármán vortices [3]–[5], galloping of certain cross-sectioned bluff bodies [6]–[14], aeroelastic flutter of flapping wings or airfoils [15]–[20], and wake galloping which involves two or more paralleled cylinders [21]–[23]. There are also other types of energy harvesters designed to mimic the behavior of a harmonica [24], cross-flow flutter behavior of a leaf [25], and the oscillatory motions of grass in turbulent flows [26]. Among these instabilities, galloping has received rapidly increasing interests. The fact that it is capable of oscillating in an infinite wind speed range above the cut-in wind speed and has large limit-cycle oscillation amplitude [27] makes it beneficial for energy harvesting purposes. In this paper, we focus on wind energy harvesting from galloping.

In order to enhance the performance of the aeroelastic energy harvesters, researchers have employed some techniques from the mechanical aspects to modify the structural designs [28]. Weinstein *et al.* [29] added a movable mass to manually tune the resonant frequency of a VIV-based harvester, achieving a broadened wind speed range with effective power generation from 2 to 5 m/s. Bibo and Daqaq [18], [19] demonstrated that an integrated airfoil flutter energy harvester under concurrent aerodynamic and base vibratory loadings had improved transduction capability and power density over two separate devices which harnessed vibration and wind energy independently. Studies on concurrent loadings have also been conducted for VIV-based harvesters [30] and galloping-based harvesters [14], [31]. Zhao *et al.* [12] proposed a 2 DOF cut-out structure with magnetic interaction which successfully enhanced the output power of a galloping harvester in the low wind speed range up to 4.5 m/s. Recently, Zhao and Yang [32] proposed an easy and effective way to increase the wind power extraction efficiency by adding a beam stiffener as an electromechanical coupling amplifier. It was shown to be effective for all three types of harvesters, i.e., harvesters based on VIV, galloping, and flutter. Nevertheless, all the above-mentioned studies mainly focus on optimizing the wind energy harvesting structures, yet simplify the interface circuit as a pure resister to consider ac output only. Since microelectronic devices like WSNs and energy storage systems require stable dc power supply, an advanced interface is needed for ac–dc conversion and power regulation. However, wind energy conversion involves complex aero-electro-mechanical coupling behaviors. The wind flows interact with the mechanical structure via aeroelasticity, and then the induced mechanical strain interacts with the electric field via the piezoelectric element through the direct electromechanical coupling. The electric field further influences the aerodynamic and mechanical aspects through

Manuscript received June 11, 2016; revised September 13, 2016 and November 8, 2016; accepted November 14, 2016. Date of publication November 18, 2016; date of current version April 14, 2017. Recommended by Technical Editor M. Basin.

L. Zhao and Y. Yang are with the School of Civil and Environmental Engineering, Nanyang Technological University, Singapore 639798 (e-mail: liyazhao@ntu.edu.sg; cywyang@ntu.edu.sg).

L. Tang is with the Department of Mechanical Engineering, University of Auckland, Auckland 1010, New Zealand (e-mail: l.tang@auckland.ac.nz).

J. Liang is with the School of Information Science and Technology, ShanghaiTech University, Shanghai 201210, China (e-mail: liangjr@shanghaitech.edu.cn).

Color versions of one or more of the figures in this paper are available online at http://ieeexplore.ieee.org.

Digital Object Identifier 10.1109/TMECH.2016.2630732

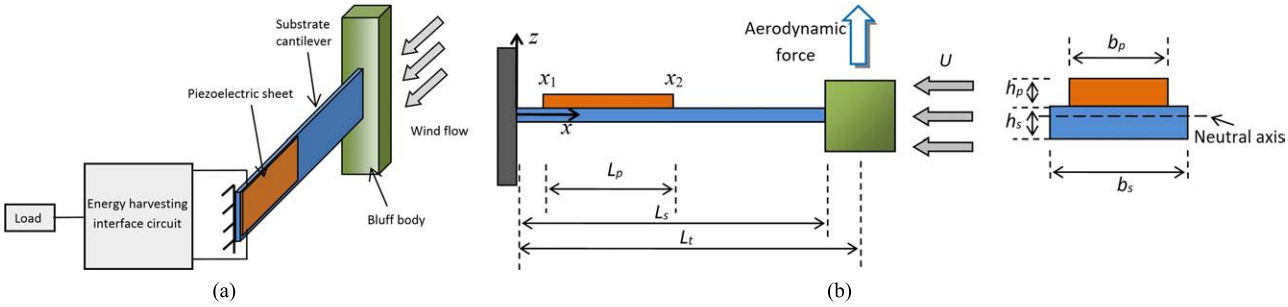

Fig. 1. (a) Configuration of a typical GPEH, (b) schematic of the GPEH geometry and the composite piezoelectric beam cross section.

backward electromechanical coupling. Therefore, the power enhancement lies not only in the structural modification, but also in the improved power extraction interface. However, although a power conditioning circuit is highly demanded, its involvement will surely complicate the mutual coupling behaviors. While various optimized nonlinear interfaces have been proposed to enhance energy harvesting from base vibrations [33]–[48], very little of such effort has been devoted to wind energy harvesting until recently [49]–[51].

Using a self-powered synchronized switch harvesting on inductor (SSHI) circuit, Liang and Liao [45] have experimentally and analytically proved that the power of an energy harvester subjected to base vibrations can be boosted up to 200% as compared to a standard circuit. This inspires the investigation of its potential in enhancing wind energy harvesting. In this paper, we employ a parallel SSHI interface circuit to enhance the power generation of a galloping piezoelectric energy harvester (GPEH). Wind tunnel experiment is carried out using a harvester prototype integrated with a built up circuit board. An analytical solution for steady-state mechanical and electrical responses under the SSHI power extraction scheme is derived explicitly and validated both experimentally and numerically. The performance of SSHI is then compared to a standard circuit under various load and wind speed conditions. The influence of electromechanical coupling on the electrical and mechanical performance is also examined.

II. Galloping Piezoelectric Energy Harvesting System

A. Aero-Electro-Mechanical Model of GPEH

A typical GPEH consists of a cantilever with a bluff body connected at its free end [Fig. 1(a)]. A piezoelectric element is bonded to the surface of the cantilever substrate near the fixed end, where the largest strain occurs during the galloping induced oscillation. The periodically alternating strain is converted into electricity via the special characteristic named "piezoelectricity." When mechanical strain is induced in the piezoelectric material, electrical charges are produced in the piezoelectric material due to the direct piezoelectric effect. This is usually called the "*sensing mode*" of piezoelectric operation [52]. The energy harvesting circuit and terminal load are connected to the electrodes of the piezoelectric element. The phenomenon of galloping was first investigated by Den Hartog [53]. It is a phenomenon of flow-induced vibration which occurs to some bluff bodies with certain cross sections. For a pure mechanical structure, when the wind speed U exceeds a threshold value, i.e., the cut-in wind speed $U_{\rm cr}$, the negative linear effective damping caused by the aerodynamic loading overcomes the intrinsic mechanical damping and as a result, the system is controlled by a negative effective damping. Self-excited oscillation arises in the direction normal to the wind flow, of which the amplitude exponentially increases with time. After a short while, the positive nonlinear damping term of the aerodynamic force dominates and brings the total effective damping back to zero. The oscillation amplitude stops increasing and remains constant, and steady-state limit-cycle oscillation is achieved. The vibration frequency is always close to the structure's first natural frequency. When the wind speed increases, the limit-cycle oscillation amplitude also increases. The characteristics of self-exciting and large range of operational wind speeds make galloping an advantageous source for energy harvesting.

Den Hartog [53] determined the criterion for galloping instability as

$$\frac{\partial C_{F_z}}{\partial \alpha} = -\frac{\partial C_l}{\partial \alpha} - C_d < 0 \tag{1}$$

where C_{F_z}, C_l, and C_d are the effective transverse galloping force coefficient, lift force coefficient, and drag force coefficient, respectively; and α is the angle of attack. Several cross-section geometries satisfy this criterion, like the square, triangular, and D-shape [27]. Our previous study [10] has shown experimentally that in laminar flows the square section performs best for wind energy harvesting. Therefore, we employ a square sectioned bluff body in the later sections of wind tunnel experiment and discussions. Yet it should be noted that the theoretical models presented in this section and the analytical solutions derived in Section III are applicable to any other cross-section geometries by utilizing the corresponding aerodynamic coefficients associated with a specific geometry.

To evaluate the mutual coupling behavior between the aerodynamic loading, mechanical structure, piezoelectric element, and interface circuit, one should establish the analytical model from two aspects, i.e., the electromechanical modeling aspect and aerodynamic modeling aspect [7], [8], [11], [32], [54]. Considering a GPEH with the schematic of geometry shown in Fig. 1(b), where a piezoelectric sheet is bonded to the beam at $x_1 < x < x_2$, the electromechanically coupled equation of

motion is built based on the Euler–Bernoulli beam theory as

$$EI_b\frac{\partial^4 w(x,t)}{\partial x^4}+c_sI_b\frac{\partial^5 w(x,t)}{\partial x^4\partial t}+c_a\frac{\partial w(x,t)}{\partial t}+m\frac{\partial^2 w(x,t)}{\partial t^2}+\theta V(t)\left[\frac{d\delta(x-x_1)}{dx}-\frac{d\delta(x-x_2)}{dx}\right]=F_{\text{galloping}}(t)\,\delta(x-L_t) \tag{2}$$

where $w(x, t)$ is the cantilever's transverse deflection along z axis; $V(t)$ is the generated voltage by the piezoelectric element; EI_b is the bending stiffness of the composite beam cross section with E and I_b being the Young's modulus and moment of inertia of cross section, respectively; c_s, c_a and m are the strain rate damping, air viscous damping and distributed mass, respectively; $F_{\text{galloping}}$ is the aerodynamic force due to galloping; L_t is the distance from the fixed end to the bluff body center; and δ is the Dirac delta function. θ is a term representing the electromechanical coupling between the mechanical and circuit aspects, expressed as $\theta = -E_p d_{31} b_p h_{\text{pc}}$ with E_p, d_{31}, b_p, and h_{pc} being the Young's modulus of the piezoelectric material, piezoelectric constant, width of the piezoelectric sheet, and position of the neutral axis of the composite beam section, respectively. The coupled circuit equation is built based on the Gauss law given by

$$I(t)+C_p\frac{dV(t)}{dt}-\theta\int_{x_1}^{x_2}\frac{\partial^3 w(x,t)}{\partial x^2\partial t}dx=0 \tag{3}$$

where $I(t)$ is the outgoing current from the piezoelectric element, and C_p is the piezoelectric capacitance.

The aerodynamic model for galloping is established based on quasi-steady hypothesis, which means that the wind loading during oscillation is regarded to be the same with that on a stationary bluff body at the same angle of attack. It is shown sufficient to model the galloping force because the characteristic timescale of the flow U/h is much smaller than the characteristic timescale of galloping oscillation, i.e., the vibration period $1/\omega_n$ [6], [27], and has successfully predicted the performance of piezoelectric galloping energy harvesters in previous wind tunnel experimental studies [7], [10]. h is the frontal width of the bluff body, and ω_n is the fundamental frequency of the harvester. $F_{\text{galloping}}$ is calculated by

$$F_{\text{galloping}}(t)=\frac{1}{2}\rho hlU^2C_{F_z}=\frac{1}{2}\rho hlU^2\sum_{i=1,2\ldots}A_i\alpha^i$$

$$\alpha=\frac{\dot{w}(L_t,t)}{U}+w'(L_t,t) \tag{4}$$

where ρ, l and A_i are the air density, length of the bluff body and empirical aerodynamic coefficients, respectively; $\dot{w}(L_t,t)$ and $w'(L_t,t)$ are the vibration velocity and rotational angle at $x = L_t$.

In order to establish the coupled modal equations, we can expand $w(x, t)$ in a convergent series of eigenfunctions as $w(x,t) = \sum\phi_r(x)\eta_r(t)$, where $\phi_r(x)$ is the rth mode shape and $\eta_r(t)$ is the modal coordinate. Here only the fundamental mode is considered, because galloping is observed to oscillate close to the structure's first natural frequency. It has been experimentally confirmed to be sufficient for accurate GPEH performance prediction [11]. Employing a mass normalization process, we can obtain the single-mode aero-electromechanically coupled model in modal coordinate η as

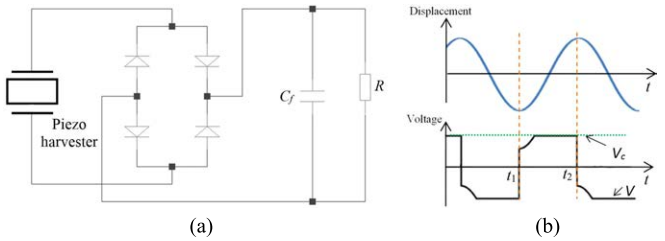

Fig. 2. (a) Standard interface circuit and (b) waveforms of voltage and tip displacement.

$$\ddot{\eta}(t)+2\zeta\omega_n\dot{\eta}(t)+{\omega_n}^2\eta(t)+\chi V(t)=f_{\text{galloping}}(t) \tag{5}$$

$$I(t)+C_p\dot{V}(t)-\chi\dot{\eta}(t)=0 \tag{6}$$

$$f_{\text{galloping}}(t)=\frac{1}{2}\phi(L_t)\rho hlU^2\sum_{i=1}^{3}A_i\left[\frac{\phi(L_t)\dot{\eta}(t)}{U}+\phi'(L_t)\eta(t)\right]^i \tag{7}$$

where ζ, χ, and $f_{\text{galloping}}$ are the mechanical damping ratio, modal electromechanical coupling coefficient as $\chi = \theta[\phi'(x_2) - \phi'(x_1)]$, and modal aerodynamic force, respectively. For more detailed model derivations of energy harvesting from various aeroelastic instabilities, interested readers are referred to the work of Sirohi and Mahadik [7], Bryant and Garcia [16], Abdelkefi *et al.* [8], De Marqui and Erturk [17], Dai *et al.* [30], Zhao and Yang [32], and Bibo *et al.* [14].

B. Interface Circuits for GPEH

During galloping vibrations, the induced strain on the piezoelectric element is alternating, thus the generated voltage is an ac output. Most researchers in the literature have focused on the conversion of wind energy to electricity and represented the interface circuit with a pure resistive load, thus, the power extraction performance is evaluated based on the ac electrical output. For practical use of the harvested wind power for small electronic devices, dc output is required. A conventional standard dc interface circuit consists of a bridge rectifier and a filtering capacitance C_f, as shown in Fig. 2(a). The rectifier is blocked when the absolute value of the piezoelectric voltage $|V|$ is less than the rectified voltage V_c across the terminal load R. Once $|V|$ reaches V_c, the rectifier conducts to transfer energy and $|V|$ is kept at V_c. Typical displacement and voltage waveforms are shown in Fig. 2(b). It should be noted that the voltage in the waveform figure represents the one across the piezoelectric element [55].

A drawback of the standard circuit is that the energy is not always flowing from the mechanical part to the electrical part [55]. With the standard circuit, for certain time duration in each half cycle the generated piezoelectric voltage and equivalent piezoelectric current are of different signs, thus, their product is negative. Nevertheless, if we employ an SSHI circuit that adds a switch S and an inductor L_i in parallel with the rectifier

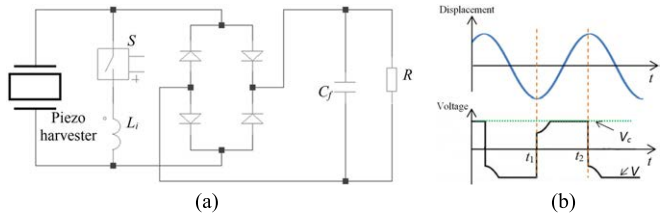

Fig. 3. (a) SSHI interface circuit and (b) waveforms of voltage and tip displacement.

as shown in Fig. 3(a), with proper switching control, we can ensure the current and piezoelectric voltage to have the same sign [33], [36], [37], [55], [56]. This is achieved by triggering the switch to induce voltage inversions only at the maximum and minimum displacement instants. The switch is kept ON only for half the formed $L_i - C_p$ cycle, i.e., $\pi\sqrt{L_i C_p}$, which is selected to be much smaller than the mechanical vibration period, thus, the voltage inversion is regarded as quasi-instantaneous. The amplitude of the instantaneous inverted voltage $|V|$ at ${t_1}^+$ is usually less than V_c, thus, the rectifier is kept blocked until $|V|$ reaches V_c. Typical waveforms of SSHI are presented in Fig. 3(b), where the voltage is the one across the piezoelectric element. For detailed operation principles of the SSHI circuit, readers are referred to [33]–[35], [45], [46]. For the aforementioned two circuits, the filter capacitor C_f, which also serves as the energy storage, is usually selected much larger than C_p, therefore, V_c, the voltage across C_f can be regarded constant.

III. Analytical Solution

Before we proceed with the derivation of the analytical solution of a GPEH connected with an SSHI interface, we introduce the following equivalent lumped parameters given by:

$$M = \frac{1}{[\phi(L_t)]^2},\ C = \frac{2\zeta\omega_n}{[\phi(L_t)]^2},$$
$$K = \frac{{\omega_n}^2}{[\phi(L_t)]^2}, \Theta = \frac{\chi}{\phi(L_t)}, u = \eta\phi(L_t) \tag{8}$$

where M, C, K, Θ, and u represent the effective mass, mechanical damping, stiffness, electromechanical coupling, and transverse displacement of the bluff body, respectively. For the aerodynamic model, it is shown that a cubic polynomial of α is sufficiently accurate to represent the galloping aerodynamic coefficient C_{F_z} with $A_1,\ A_3 \neq 0$, and $A_2 = 0$ for a symmetrical cross section [6], [27]. Incorporating the above parameters, the single-mode distributed parameter aero-electro-mechanical model can be degraded into

$$M\ddot{u} + C\dot{u} + Ku + \Theta V = F_{\text{galloping}}$$
$$= \frac{1}{2}\rho h L U^2 \left[A_1\left(\frac{\dot{u}}{U} + \beta u\right) + A_3\left(\frac{\dot{u}}{U} + \beta u\right)^3\right] \tag{9}$$

$$I + C_p\dot{V} - \Theta\dot{u} = 0 \tag{10}$$

where β is calculated by $\beta = \phi'(L_t)/\phi(L_t)$. For convenient formulation and quick comparison of different harvester configurations, the next step analytical solutions are derived based on (9) and (10). Yet it should be noted that, although (9) and (10) are in the form of a lumped parameter model [11], it is equivalent to the single-mode distributed parameter model because the lumped parameters are equivalent substitutions of the distributed parameters from modal calculations.

At time instants t_1 and t_2, $u(t)$ reaches its minimum and maximum, respectively [Fig. 3(b)]. The voltage inversion is supposed to be quasi-instantaneous, with the switch being conducted for a very short time interval from t_1 to t_1^+. During $[t_1,\ t_1^+]$, some energy loss is induced by the imperfect inversion in the switch-$L_i - C_p$ loop, of which the quality factor is Q. When the switch is OFF again at t_1^+, the inverted piezoelectric voltage V is less than V_c, expressed as

$$V\left({t_1}^+\right) = \gamma V_c = -V\left(t_1\right)e^{\frac{-\pi}{2Q}}$$
$$\gamma = e^{\frac{-\pi}{2Q}} \tag{11}$$

where γ is the voltage inversion factor with $0 < \gamma \leq 1$. $\gamma = 1$ denotes the extreme condition with ideal inversion. To obtain the relation between the rectified voltage V_c and the displacement magnitude u_m, we consider the charging balance in the whole system. During steady-state oscillations, the current flowing through C_f is zero, thus we have

$$\int_{{t_1}^+}^{t_2} I(t)dt = \frac{V_c}{R}\frac{T}{2}. \tag{12}$$

Inspecting the displacement and voltage values at the two instants t_1^+ and t_2, we obtain

$$\int_{{t_1}^+}^{t_2}\left[-C_p\dot{V}(t) + \Theta\dot{u}(t)\right]dt = -C_p(1-\gamma)V_c + 2\Theta u_m. \tag{13}$$

Considering (10), the right hand sides of (12) and (13) should be equal, yielding the relation between V_c and u_m as

$$V_c = \frac{2\Theta R\omega}{\pi + C_p\left(1-\gamma\right)R\omega}u_m. \tag{14}$$

Next, to obtain the explicit expression of u_m and V_c, we employ the equations of energy balance and follow a similar procedure to that of Shu *et al.* [36]. Multiplying (9) by $\dot{u}$ and (10) by V, and integrating the obtained equations over half vibration period $[t_1^+,\ t_2]$ yield

$$\int_{{t_1}^+}^{t_2} F_{\text{galloping}}\dot{u}dt = \frac{1}{2}M\dot{u}^2\Big|_{{t_1}^+}^{t_2} + \frac{1}{2}Ku^2\Big|_{{t_1}^+}^{t_2} + \int_{{t_1}^+}^{t_2} C\dot{u}^2dt + \int_{{t_1}^+}^{t_2}\Theta V\dot{u}dt \tag{15a}$$

$$\int_{{t_1}^+}^{t_2} IVdt + \frac{1}{2}C_pV^2\Big|_{{t_1}^+}^{t_2} = \int_{{t_1}^+}^{t_2}\Theta V\dot{u}dt. \tag{15b}$$

The terms in (15a) are, respectively, the input energy by the aerodynamic force, kinetic energy, elastic potential energy, mechanical damping induced energy loss, and transferred electrical energy; and the first two terms in (15b) are, respectively,

the energy extracted by the interface circuit and the electrostatic energy accumulated on the piezoelectric capacitance. We assume that the displacement during steady-state oscillations has the form of

$$u(t) = -u_m \cos(\omega t). \tag{16}$$

With this expression, by setting $t_1 = 0$ and $t_2 = T/2$, $u(t)$ achieves $-u_m$ and u_m at the two instants. Again, inspecting Fig. 3(b), it is seen that the kinetic energy is zero at t_1 and t_2, and the elastic energy does not vary during the half period, i.e., $\frac{1}{2}M\dot{u}^2\big|_{0^+}^{\frac{T}{2}} = 0$, and $\frac{1}{2}Ku^2\big|_{0^+}^{\frac{T}{2}} = 0$. The equation of energy balance in (15) can be rewritten as

$$\int_{0^+}^{\frac{T}{2}} F_{\text{galloping}}\dot{u}dt = \int_{0^+}^{\frac{T}{2}} C\dot{u}^2 dt + \int_{0^+}^{\frac{T}{2}} IV dt + \int_{0^+}^{\frac{T}{2}} C_p\dot{V}V dt \tag{17}$$

where in steady-state operation the energy extracted by the circuit is

$$\int_{0^+}^{\frac{T}{2}} IV dt = \frac{{V_c}^2}{R}\frac{T}{2} \tag{18}$$

and the rest of the transferred energy is the electrostatic energy in the piezoelectric element

$$\int_{0^+}^{\frac{T}{2}} C_p\dot{V}V dt = \frac{1}{2}C_p{V_c}^2\left(1-\gamma^2\right). \tag{19}$$

Now substituting (16) into (17) gives

$$\begin{aligned}&\frac{1}{2}C\omega\pi{u_m}^2 + \left[\frac{\pi}{R\omega} + \frac{1}{2}C_p\left(1-\gamma^2\right)\right]{V_c}^2 \\ &= \frac{1}{2}\rho hLU^2{u_m}^2\left[\frac{A_1\omega\pi}{2U} + \frac{3A_3\omega\pi}{8U}\left(\frac{\omega^2}{U^2}+\beta^2\right){u_m}^2\right].\end{aligned} \tag{20}$$

Introducing the relation between V_c and u_m that has been obtained in (14), u_m can be explicitly expressed as

$$u_m = \sqrt{\frac{\frac{1}{2}C\omega\pi + \frac{4\Theta^2\left[\frac{\pi}{R\omega}+\frac{1}{2}C_p(1-\gamma^2)\right]}{\left[\frac{\pi}{R\omega}+C_p(1-\gamma)\right]^2} - \frac{1}{4}\rho hLUA_1\omega\pi}{\frac{3}{16}\rho hLUA_3\omega\pi\left(\frac{\omega^2}{U^2}+\beta^2\right)}}. \tag{21}$$

And it is straightforward to obtain the final average output power based on (14) as

$$P_{\text{ave}} = \frac{{V_c}^2}{R} = \frac{4\Theta^2 R\omega^2}{\left[\pi + 2C_p(1-\gamma R\omega)\right]^2}{u_m}^2. \tag{22}$$

The displacement, voltage, and power can be further normalized for convenient parametric studies and fair comparison between various harvesters and interfaces, with the nondimensional parameters given by

$$\hat{M} = \frac{M}{\rho h^2 L}, \hat{U} = \frac{U}{\omega_n h}, {k_e}^2 = \frac{\Theta^2}{C_p K}, \Omega = \frac{\omega}{\omega_n}, r = C_p R\omega_n \tag{23}$$

where $\hat{M}$ and $\hat{U}$ are the dimensionless mass ratio and reduced wind speed, respectively; and k_e, Ω and r are the alternative electromechanical coupling coefficient, normalized frequency and resistive load, respectively. The normalized responses are written as

$$\hat{u}_m = \frac{u_m}{h} = \sqrt{\frac{\zeta - \frac{1}{4}\frac{\hat{U}}{\hat{M}}A_1 + \frac{4{k_e}^2\left(\frac{1}{r\Omega^2}+\frac{1-\gamma^2}{2\pi\Omega}\right)}{\left[\frac{\pi}{r\Omega}+(1-\gamma)\right]^2}}{\frac{3}{16}\frac{\hat{U}}{\hat{M}}A_3\left(\frac{\Omega^2}{\hat{U}^2}+\beta^2h^2\right)}} \tag{24}$$

$$\begin{aligned}\hat{P}_{\text{ave}} &= \frac{P_{\text{ave}}}{M{\omega_n}^3h^2} = \frac{4{k_e}^2}{r\left[\frac{\pi}{r\Omega}+(1-\gamma)\right]^2} \\ &\cdot \frac{\zeta - \frac{1}{4}\frac{\hat{U}}{\hat{M}}A_1 + \frac{4{k_e}^2\left(\frac{1}{r\Omega^2}+\frac{1-\gamma^2}{2\pi\Omega}\right)}{\left[\frac{\pi}{r\Omega}+(1-\gamma)\right]^2}}{\frac{3}{16}\frac{\hat{U}}{\hat{M}}A_3\left(\frac{\Omega^2}{\hat{U}^2}+\beta^2h^2\right)}.\end{aligned} \tag{25}$$

The analytical solution for a GPEH with the standard interface (see Fig. 2) has been derived by Zhao and Yang [49]. The results are quoted here for comparison with the SSHI circuit:

$$\hat{u}_m = \frac{1}{h\sqrt{\frac{\Omega^2}{\hat{U}^2h^2}+\beta^2}}\sqrt{\frac{\zeta\Omega + \frac{4{k_e}^2r\Omega}{(\pi+2r\Omega)^2} - \frac{1}{4}A_1\Omega\frac{\hat{U}}{\hat{M}}}{\frac{3}{16}A_3\Omega\frac{\hat{U}}{\hat{M}}}} \tag{26}$$

$$\begin{aligned}\hat{P}_{\text{ave}} &= \frac{4{k_e}^2r\Omega^2}{(\pi+2r\Omega)^2}\frac{1}{h^2\left(\frac{\Omega^2}{\hat{U}^2h^2}+\beta^2\right)} \\ &\cdot \frac{\zeta\Omega + \frac{4{k_e}^2r\Omega}{(\pi+2r\Omega)^2} - \frac{1}{4}A_1\Omega\frac{\hat{U}}{\hat{M}}}{\frac{3}{16}A_3\Omega\frac{\hat{U}}{\hat{M}}}.\end{aligned} \tag{27}$$

The normalized frequency is influenced by both the resistive load and wind speed, and its variation has also been determined in the previous study [49]. In the following calculations, Ω is regarded as the open-circuit resonance frequency Ω_{oc} considering that for a certain portion of each cycle the rectifier is blocked during which the circuit experiences open-circuit condition.

IV. Experimental Setup and Circuit Simulation

Wind tunnel experiment and circuit simulation are carried out to validate the derived analytical solution in Section III. A GPEH prototype is fabricated with an aluminum cantilever connected with a square sectioned bluff body at the free end, as shown in Fig. 4(a). The other end of the cantilever is clamped into a metal support to achieve a fixed boundary condition. A piece of piezoelectric element (MFC M2814-P2 from Smart Materials Corporation) is attached to the root area of the cantilever where the largest strain energy occurs during vibrations. The geometrical, mechanical, and electrical properties of the cantilever and piezoelectric element are listed in Table I. The bluff body is made of polystyrene foam, with a cross section of 20×20 mm^2, a length of 100 mm and a weight of 1.8 g. The short circuit fundamental frequency of the harvester is measured to be 16.67 Hz. The damping ratio is tested from the logarithmic decrement technique to be 0.011. During the experiment the harvester is installed in the wind tunnel with the front of the bluff body facing the wind flow, as shown in Fig. 4(b). The air

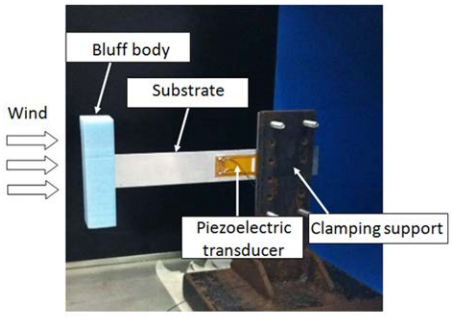

(a)

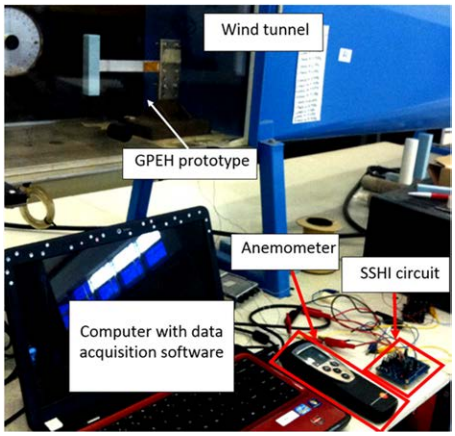

(b)

Fig. 4. (a) Fabricated harvester prototype and (b) overall experimental setup in the wind tunnel.

TABLE I
PROPERTIES OF PIEZOELECTRIC CANTILEVER OF GPEH

Properties	Cantilever substrate	Piezoelectric element
Length L_s, L_p (mm)	130	28
Width b_s, b_p (mm)	20	14
Thickness h_s, h_p (mm)	0.6	0.3
Mass density (kg m^{-3})	2700	5440
Young's modulus E_s, E_p (GPa)	69	30.336
Capacitance C_p (nF)	–	25.7
Piezoelectric constant d_{31} pm/V	–	−170
Material	Aluminum	MFC M2814-P2

temperature is 20 °C thus the air density is taken as 1.204 kg/m^3. The wind speed is measured with a hotwire anemometer.

A circuit hardware is built up and connected to the piezoelectric electrodes. The circuit schematic is shown in the right rectangle of Fig. 5, which incorporates the self-powered SSHI interface. In an externally powered SSHI, to implement the switching action, additional displacement sensor and switch controller are indispensable. In order to remove the requirement of additional power supplier, displacement maxima detection and switching have been designed to be self-powered [38], [42], [48] using the electronic breaker composed of the envelope detector, comparator, and switch components [57]. An improved electronic breaker pair was proposed by Liang and Liao [45] with a complementary transistor topology. It removed all the energy consuming isolating resistors, in the meanwhile, better envelope detection of the piezoelectric voltage and reduction of the interference among different components were achieved by the self-powered circuit. During the test, the voltage across the piezoelectric element and the terminal load is measured by the NI 9229 DAQ module from National Instruments together with LabVIEW. The models and values of the circuit components are listed in Table II.

In addition to the wind tunnel experiment, circuit simulation is also conducted based on the equivalent circuit model of the GPEH. By analogizing the mechanical parameters as the electrical parameters, i.e., analogizing u, $\dot{u}$, M, C, K, and Θ as the charge q, current $\dot{q}$, inductor L_0, resistor R_0, reciprocal of capacitor C_0, and turn ratio N of the ideal transformer, respectively, the GPEH structure can be represented by the equivalent circuit shown in the left rectangle of Fig. 5. The aerodynamic galloping force is represented by a user defined arbitrary voltage source. Detailed derivations are provided in Tang *et al.* [58]. Integrating the equivalent circuit model with the self-powered SSHI circuit employed during experiment, system-level circuit simulation can be carried out.

V. RESULTS AND DISCUSSION

A. Validation of Analytical Solutions

Before proceeding with the experimental and numerical validations of the analytical solutions, one more issue on the energy loss needs to be clarified. During the analytical derivation, the transferred electrical energy is considered to have two parts, the harvested energy by the circuit in (18) and dissipated energy in (19). The energy dissipation results from the nonideal voltage inversion process. For ideal voltage inversion, the quality factor $Q = \infty$. Yet in a practical situation, the parasitic resistance in the switching path affects Q and causes $\gamma < 1$. Therefore, the energy dissipation in (19) always exists. In the experiment and circuit simulation, due to the employment of self-powered switching components, more energy loss would be incurred. The diodes and transistors involved in the electronic breakers induce extra voltage drops, resulting in extra energy loss. Moreover, the equivalent piezoelectric resistance (not represented in the circuit diagram) that is parallel to C_p would induce extra piezoelectric dielectric loss. These two types of energy losses are not considered in the analytical derivation. Also, as has been determined by Liang and Liao [44], the piezoelectric dielectric loss causes a slight voltage reversion phenomenon right after the voltage inversion. Such voltage reversion is also neglected in the analytical derivation. This may account for the discrepancies among the experimental and numerical results and the analytical solutions.

The quality factor for the developed prototype is measured from the recorded voltage signal to be $Q = 2.9$ using (11). This value is employed for the calculations in the present and following sections. During the circuit simulation and analytical calculation, the empirical aerodynamic coefficients are taken as $A_1 = 2.3$, $A_2 = 0$, and $A_3 = -18$ [6]. It should be noted that A_3 being negative ensures that a positive nonlinear damping term of the aerodynamic force is brought into the vibration system, self-limiting the galloping amplitude and mak-

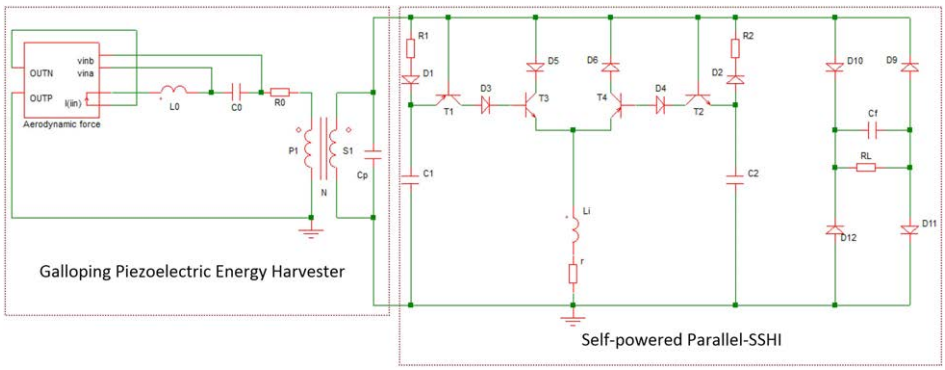

Fig. 5. Equivalent circuit model of the GPEH connected with a self-powered SSHI circuit.

TABLE II
CIRCUIT COMPONENT VALUES

Component	Model/Value
R_1 and R_2 (kΩ)	200
C_1 and C_2 (pF)	680
Diodes (D_1 to D_{12})	1N4004
PNP transistors (T_1 and T_4)	TIP32C
NPN transistors (T_2 and T_3)	TIP31C
C_f (μF)	20
L_i (mH)	47
r (Ω)	460

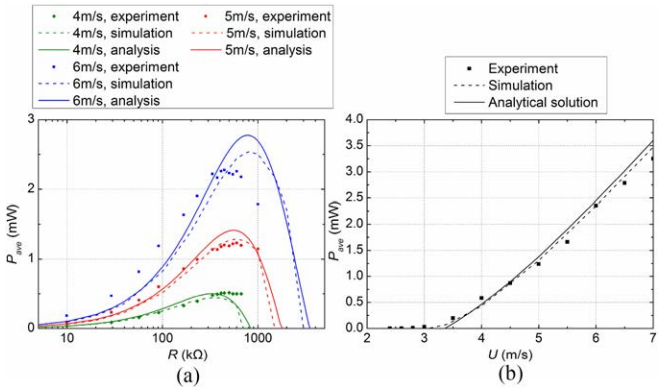

Fig. 6. Comparison of results of SSHI interface from wind tunnel experiment, circuit simulation, and analytical solution. (a) Average power versus load resistance at different wind speeds. (b) Average power versus wind speed at $R = 445$ kΩ.

ing the harvester undergo steady-state limit-cycle oscillation at each wind speed. The variations of the output power from experiment, simulation, and analytical solutions as functions of load resistance and wind speed are plotted in Fig. 6. It is seen from Fig. 6(a) that at each wind speed U, there exists an optimal load resistance R at which the output power reaches maximum. The optimal R is not constant but varies with the wind speeds. When U increases, the optimal R also increases. Reasonable agreement is observed between the experiment, simulation, and analytical results. Besides the source of discrepancies discussed above, the inevitable turbulence in the wind tunnel and increasing energy loss in the switching path at high wind speeds would also account for the discrepancies. In Fig. 6(b), a constant R of

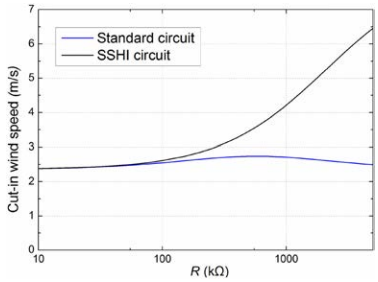

Fig. 7. Variation of cut-in wind speed of GPEH with load resistance with standard and SSHI circuits.

445 kΩ is employed for the considered range of U. It is seen that the output power from the GPEH with an SSHI circuit monotonically increases with the wind speed due to the increasing input aerodynamic force. Good agreement is obtained between the analysis and the experimental and numerical results in both the cut-in wind speed and power level.

B. Performance Comparison Between SSHI and Standard Interfaces

With the validated analytical solution, the electrical and mechanical performance of a GPEH integrated with the SSHI circuit is evaluated and compared with a standard circuit. The variations of the cut-in wind speed, mechanical displacement which reflects the electrical damping effect, and output power are investigated. The influences of electromechanical coupling on the output power and mechanical displacement are evaluated. In order to obtain a dimensional understanding of the harvester's performance, in the following analysis, dimensional parameters are utilized.

1) Cut-in Wind Speed Comparison: The variation of cut-in wind speed as a function of the load resistance is shown in Fig. 7 for the standard and SSHI circuits. The harvester and circuit parameters employed in the analysis are the same with those of the fabricated prototype. In such a case, the dimensionless electromechanical coupling coefficient square $k_e{}^2$ is determined to be 0.01136. With $\zeta = 0.011$, it is calculated that $k_e{}^2/\zeta = 1.033$, which has been determined to be within the weak coupling range for the considered wind speeds [49], [50]. With the standard circuit, the cut-in speed first increases with

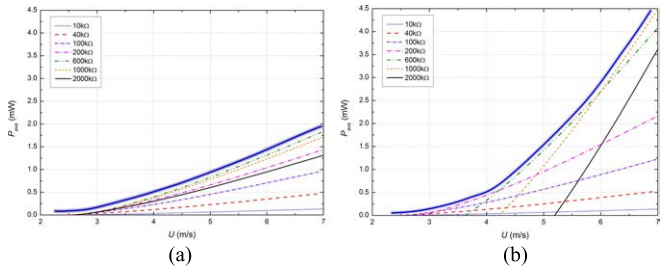

Fig. 8. Variation of output power of GPEH with wind speed (a) standard circuit and (b) SSHI circuit. The bold solid curve denotes the envelope of attainable output power with the respective interface.

TABLE III
POWER ENHANCEMENT

Wind speed (m/s)	Power (mW)		Enhancement percentage
	SSHI	Standard	
3	0.06	0.06	0
4	0.44	0.40	10%
5	1.41	0.83	70%
6	2.69	1.32	104%
7	4.48	1.84	143%

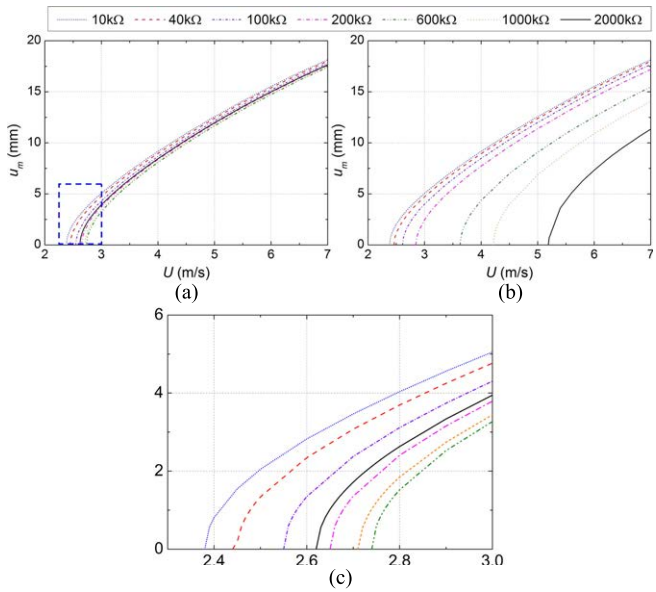

Fig. 9. Variation of transverse displacement at tip of GPEH with wind speed (a) standard circuit, (b) SSHI circuit, and (c) enlarged view of standard circuit response in the dashed box.

R to a maximum, then decreases when R further increases. In contrast, the cut-in speed with SSHI monotonically increases with R. The increasing rate over the small and medium R range (10–300 kΩ) is relatively small. Within this range, the cut-in speed with SSHI stays between 2.3–3.0 m/s and is comparable to that with the standard circuit. When R becomes larger, the SSHI induces larger electrical damping, thus requires higher wind speeds for galloping oscillation to occur than the standard circuit does. This is also reflected in Fig. 6(a) that the harvester gives no output power when R is beyond a certain value for a specific wind speed, e.g., there is no power for $R = 1000$ kΩ at $U = 4$ m/s, since this wind speed is smaller than the cut-in speed of 4.2 m/s for 1000 kΩ. However, the enlarged electrical damping of SSHI expects the enhanced power generation capability, which will be confirmed in the following section.

2) Output Power Comparison: Fig. 8 compares the variations of output power as functions of wind speed for the two circuits at various load resistances. It is clearly noted by the bold solid power envelopes that significant power enhancement is achieved with SSHI over the standard circuit. As seen from Fig. 8(a), for the standard circuit, the increasing rate of power with wind speed, i.e., the slope of the $P_{\text{ave}} - U$ curve, first increases with R and then decreases. In contrast, Fig. 8(b) shows that the power increasing rate for SSHI monotonically increases with R. As a result, the power enhancement of SSHI over standard circuit gets more pronounced with the increasing wind speed. For instance, at the respective optimal R, the output power at a small wind speed of 4.5 m/s is increased from 0.60 mW with the standard circuit to 0.84 mW with SSHI, corresponding to a 40% enhancement. At a medium wind speed of 5.5 m/s, the power is increased from 1.07 to 2.03 mW with a 90% enhancement. At a relatively high wind speed of 7 m/s, up to 143% power enhancement is obtained from 1.84 to 4.48 mW. Quantitative comparisons for other wind speeds are listed in Table III.

These results confirm the superiority of SSHI over the standard circuit in wind power extraction via the synchronized voltage inversion with the mechanical displacement.

3) Tip Displacement (Damping Effect) Comparison: The responses of the transverse displacement at the harvester tip are compared in Fig. 9 for different wind speeds and load resistances. The variation of the cut-in wind speed is also reflected by the intersection points of the curves with the horizontal axis. It is seen more clearly that at relatively small R, the two circuits have comparable cut-in speeds, while at relatively large R, the SSHI requires higher cut-in speeds. In terms of the displacement amplitude at each wind speed, the SSHI results in comparable displacement with the standard circuit at small R, while at large R, the displacement with SSHI is obviously smaller. Therefore, with the enhanced output power, the SSHI also beneficially brings down the displacement which helps to alleviate the fatigue problem for the harvester structure during the wind-induced oscillations. Moreover, the smaller displacement confirms the stronger electrical damping and better energy conversion of SSHI.

4) Influence of Coupling Strength: We move on to investigate the influence of the strength of electromechanical coupling on the harvester's responses with the SSHI interface. Three different values of k_e^2/ζ are considered which correspond to a weak, medium, and strong coupling condition, respectively. First, we consider the parameters of the experiment prototype which give $k_e^2/\zeta = 1.033$ with $k_e^2 = 0.01136$ and $\zeta = 0.011$. The variation of power with load resistance at different wind speeds is shown in Fig. 10(a) with the standard circuit and in Fig. 10(b) with SSHI. Significant power increase is observed with SSHI over the standard circuit. For example, as compared to the standard circuit, at $U = 5$ m/s, 6 m/s, and 7 m/s, the power is increased by SSHI from 0.83 to 1.42 mW, from 1.32 to 2.76 mW, and from 1.84 to 4.48 mW, respectively. These correspond to 71%, 109%, and 143% enhancements, respec-

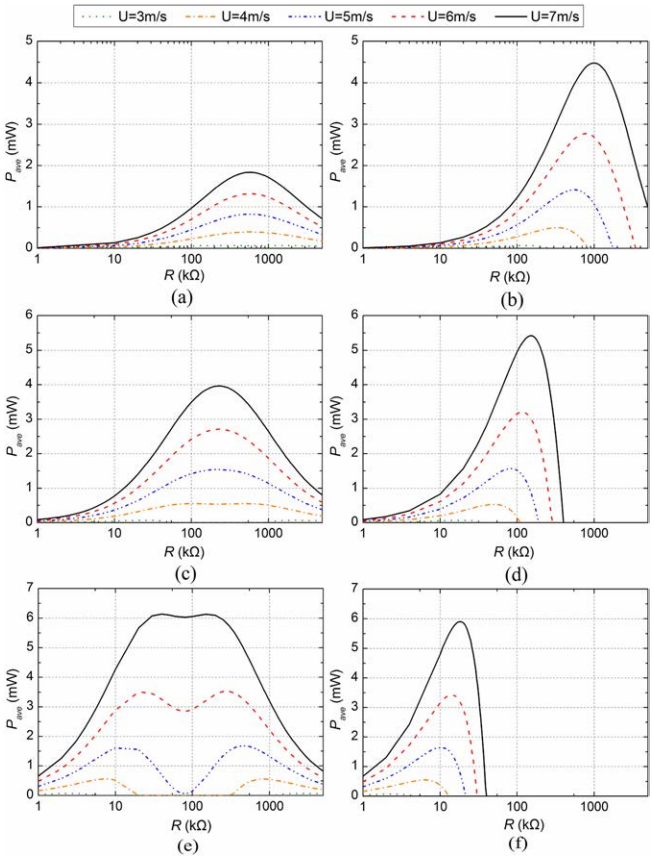

Fig. 10. Variation of output power with load resistance at different wind speeds with (a), (c), and (e) standard circuit and (b), (d), and (f) SSHI. Electromechanical coupling strength: (a) and (b) $k_e^2/\zeta = 1.033$, (c) and (d) $k_e^2/\zeta = 2.545$, and (e) and (f) $k_e^2/\zeta = 7.273$.

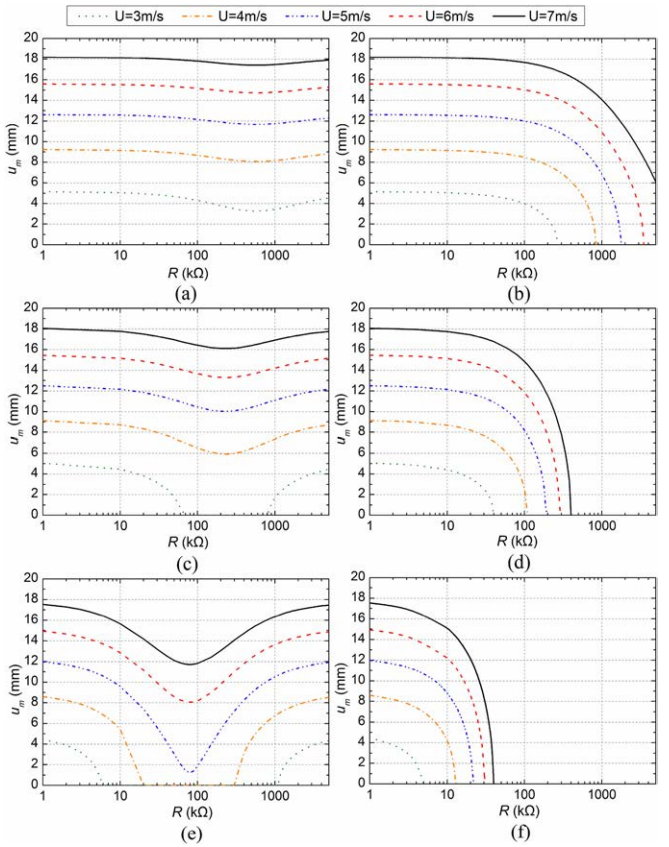

Fig. 11. Variation of transverse displacement with load resistance at different wind speeds with (a), (c), and (e) standard circuit and (b), (d), and (f) SSHI. Electromechanical coupling strength: (a) and (b) $k_e^2/\zeta = 1.033$, (c) and (d) $k_e^2/\zeta = 2.545$, and (e) and (f) $k_e^2/\zeta = 7.273$.

tively. Unlike the case with the standard circuit that the optimal R for maximum power keeps almost constant at different U, the optimal R with SSHI monotonically increases with U.

Next, the coupling is theoretically assumed to increase to a medium range with $k_e^2/\zeta = 2.545$ ($k_e^2 = 0.028$ and $\zeta = 0.011$), which can be realized by attaching more piezoelectric sheets onto the cantilever substrate in practice [56]. The results are shown in Fig. 10(c) and (d). It is seen that, as compared to the weak coupling case, the power enhancement percentage is decreased. Compared to that with standard circuit, the power is increased by SSHI from 1.54 mW, 2.70 mW, and 3.96 mW to 1.56 mW, 3.21 mW, and 5.42 mW at $U = 5$ m/s, 6 m/s, and 7m/s, respectively, corresponding to 1.3%, 19%, and 37% enhancements, respectively.

Finally, we assume a strong coupling of $k_e^2/\zeta = 7.273$ with $k_e^2 = 0.080$ and $\zeta = 0.011$. In this condition, it has been determined by Zhao and Yang [49] that the harvester with a standard circuit has entered the strong coupling range showing power saturation for the considered wind speeds. The results for the standard circuit are shown in Fig. 10(e) and for SSHI in Fig. 10(f). With the standard circuit, two identical power peaks occur at each U with a valley in between. Inspecting the corresponding displacement shown in Fig. 11(e), we can see that this valley of power corresponds to the valley of displacement, indicating that the R in the power valley still induces the largest electrical damping. With the SSHI, there is only one peak power. Comparing the power levels, it is seen that the SSHI gives equal maximum power with the standard circuit at each U in this strong coupling condition. However, a disadvantage is revealed for the SSHI. At this strong coupling, the power with SSHI becomes very sensitive to the deviation of R around the peak. A slight shift of R beyond the optimal value results in a significant power drop. This is very likely to happen considering the components induced electrical damping involved in the terminal load circuit. Due to this issue, the SSHI is no longer beneficial in a strong coupling case. In addition, revisiting the power levels of SSHI at weak coupling in Fig. 10(b) and comparing them with those in Fig. 10(e), it is found that a weak-coupling system (much less piezoelectric material used) connected to the SSHI can achieve similar power to that of a strong-coupling system connected to the standard circuit. This conclusion is consistent with the one drawn by Shu *et al.* [36] for vibration energy harvesting enhanced by the SSHI. This achievement further proves the power boosting benefits of SSHI for a weak coupling system and its advantage of saving piezoelectric materials.

The responses of transverse displacement at different coupling conditions are further compared in Fig. 11. For both circuits, increasing the coupling results in reduced displacement. Generally, the displacement with SSHI is smaller than that with the standard circuit due to the higher electrical damping. Unlike the case with the standard circuit that a valley of displacement occurs in the middle range of R, the displacement with SSHI

monotonically decreases with R. Moreover, it is noticed by comparing Figs. 11(b), (d), and (f) to 10(b), (d), and (f) that when R is far away from the power peak, the displacement variation is negligible, while when R continues to increase around the power peak, the displacement decreases quickly, which indicates the fast increasing electrical damping around the power peak. Finally, it is worth noting that at strong coupling, the cut-in speed with SSHI is highly sensitive to the variation of R. This makes the use of SSHI very risky because a small change of wind speed in the environment may result in no output power. As a result, it should be stressed that the SSHI is not recommended in a strong electromechanically coupled galloping harvester system.

VI. Conclusion

This paper analyzes the power enhancing performance of the SSHI circuit in a galloping piezoelectric energy harvesting system. It is found that in a system with weak electromechanical coupling, the SSHI can tremendously enhance the output power over the standard circuit. The higher the wind speed, the more pronounced the power enhancement is. Considering a quality factor of 2.9 in the switching path, at a wind speed of 7 m/s, the SSHI can harvest up to 143% more power than the standard circuit. Due to the higher electrical damping, the SSHI induces smaller transverse displacement than the standard circuit, which beneficially mitigates the structural fatigue of the harvester. Further analysis of the influence of the strength of electromechanical coupling on the harvester's responses reveals that the advantage of SSHI is more prominent at weak coupling scenario. With the SSHI, a weak-coupling system with much less piezoelectric material can achieve similar power to that of a strong-coupling system connected to a standard circuit, helping to save piezoelectric materials. Increasing the coupling reduces the power enhancement percentage of SSHI over the standard circuit. In special, in the strong coupling condition, the output power and cut-in wind speed with SSHI are very sensitive to the deviation of R, which makes the utilization of SSHI very risky considering the possible change of load in a terminal circuit or possible variation of wind speed in the environment. It is concluded that SSHI enhances the energy harvesting performance of and is suitable for weak-coupling and medium-coupling systems.

References

[1] S. Priya, "Modeling of electric energy harvesting using piezoelectric windmill," *Appl. Phys. Lett.*, vol. 87, 2005, Art. no. 184101.

[2] M. A. Karami, J. R. Farmer, and D. J. Inman, "Parametrically excited nonlinear piezoelectric compact wind turbine," *Renew. Energy*, vol. 50, pp. 977–987, 2013.

[3] S. Pobering, M. Menacher, S. Ebermaier, and N. Schwesinger, "Piezoelectric power conversion with self-induced oscillation," in *Proc. PowerMEMS*, 2009, pp. 384–387.

[4] H. D. Akaydin, N. Elvin, and Y. Andreopoulos, "The performance of a self-excited fluidic energy harvester," *Smart Mater. Struct.*, vol. 21, 2012, Art. no. 025007.

[5] X. Gao, W.-H. Shih, and W. Y. Shih, "Flow energy harvesting using piezoelectric cantilevers with cylindrical extension," *IEEE Trans. Ind. Electron.*, vol. 60, no. 3, pp. 1116–1118, Mar. 2013.

[6] A. Barrero-Gil, G. Alonso, and A. Sanz-Andres, "Energy harvesting from transverse galloping," *J. Sound Vib.*, vol. 329, pp. 2873–2883, 2010.

[7] J. Sirohi and R. Mahadik, "Piezoelectric wind energy harvester for low-power sensors," *J. Intell. Mater. Syst. Struct.*, vol. 22, pp. 2215–2228, 2011.

[8] A. Abdelkefi, Z. Yan, and M. R. Hajj, "Modeling and nonlinear analysis of piezoelectric energy harvesting from transverse galloping," *Smart Mater. Struct.*, vol. 22, 2013, Art. no. 025016.

[9] Z. Yan and A. Abdelkefi, "Nonlinear characterization of concurrent energy harvesting from galloping and base excitations," *Nonlinear Dyn.*, vol. 77, pp. 1171–1189, 2014.

[10] Y. Yang, L. Zhao, and L. Tang, "Comparative study of tip cross-sections for efficient galloping energy harvesting," *Appl. Phys. Lett.*, vol. 102, 2013, Art. 064105.

[11] L. Zhao, L. Tang, and Y. Yang, "Comparison of modeling methods and parametric study for a piezoelectric wind energy harvester," *Smart Mater. Struct.*, vol. 22, 2013, Art. no. 125003.

[12] L. Zhao, L. Tang, and Y. Yang, "Enhanced piezoelectric galloping energy harvesting using 2 degree-of-freedom cut-out cantilever with magnetic interaction," *Jpn. J. Appl. Phys.*, vol. 53, 2014, Art. no. 060302.

[13] F. Ewere, G. Wang, and B. Cain, "Experimental investigation of galloping piezoelectric energy harvesters with square bluff bodies," *Smart Mater. Struct.*, vol. 23, 2014, Art. no. 104012.

[14] A. Bibo, A. Abdelkefi, and M. F. Daqaq, "Modeling and characterization of a piezoelectric energy harvester under combined aerodynamic and base excitations," *J. Vib. Acoust. Trans. ASME*, vol. 137, 2015, Art. 031017.

[15] Q. Zhu and Z. Peng, "Mode coupling and flow energy harvesting by a flapping foil," *Phys. Fluids*, vol. 21, 2009, Art. no. 033601.

[16] M. Bryant and E. Garcia, "Modeling and testing of a novel aeroelastic flutter energy harvester," *J. Vib. Acoust. Trans. ASME*, vol. 133, 2011, Art. no. 011010.

[17] C. De Marqui and A. Erturk, "Electroaeroelastic analysis of airfoil-based wind energy harvesting using piezoelectric transduction and electromagnetic induction," *J. Intell. Mater. Syst. Struct.*, vol. 24, pp. 846–854, 2012.

[18] A. Bibo and M. F. Daqaq, "Investigation of concurrent energy harvesting from ambient vibrations and wind using a single piezoelectric generator," *Appl. Phys. Lett.*, vol. 102, 2013, Art. no. 243904.

[19] A. Bibo and M. F. Daqaq, "Energy harvesting under combined aerodynamic and base excitations," *J. Sound Vib.*, vol. 332, pp. 5086–5102, 2013.

[20] Y. Wang and D. Inman, "Experimental validation for a multifunctional wing spar with sensing, harvesting, and gust alleviation capabilities," *IEEE/ASME Trans. Mechatronics*, vol. 18, no. 4, pp. 1289–1299, Aug. 2013.

[21] H.-J. Jung and S.-W. Lee, "The experimental validation of a new energy harvesting system based on the wake galloping phenomenon," *Smart Mater. Struct.*, vol. 20, 2011, Art. 055022.

[22] W. B. Hobbs and D. L. Hu, "Tree-inspired piezoelectric energy harvesting," *J. Fluid. Struct.*, vol. 28, pp. 103–114, 2012.

[23] A. Abdelkefi, J. M. Scanlon, E. McDowell, and M. R. Hajj, "Performance enhancement of piezoelectric energy harvesters from wake galloping," *Appl. Phys. Lett.*, vol. 103, 2013, Art. no. 033903.

[24] A. Bibo, G. Li, and M. F. Daqaq, "Performance analysis of a harmonicatype aeroelastic micropower generator," *J. Intell. Mater. Syst. Struct.*, vol. 23, pp. 1461–1474, 2012.

[25] S. Li, J. Yuan, and H. Lipson, "Ambient wind energy harvesting using cross-flow fluttering," *J. Appl. Phys.*, vol. 109, 2011, Art. no. 026104.

[26] J. D. Hobeck and D. J. Inman, "Artificial piezoelectric grass for energy harvesting from turbulence-induced vibration," *Smart Mater. Struct.*, vol. 21, 2012, Art. 105024.

[27] M. P. Païdoussis, S. J. Price, and E. De Langre, *Fluid-Structure Interactions: Cross-Flow-Induced Instabilities*. New York, NY, USA: Cambridge Univ. Press, 2010.

[28] L. Zhao, "Small-scale wind energy harvesting using piezoelectric materials," Ph.D. thesis, Nanyang Technol. Univ., Singapore, 2015.

[29] L. A. Weinstein, M. R. Cacan, P. M. So, and P. K. Wright, "Vortex shedding induced energy harvesting from piezoelectric materials in heating, ventilation and air conditioning flows," *Smart Mater. Struct.*, vol. 21, 2012, Art. no. 045003.

[30] H. Dai, A. Abdelkefi, and L. Wang, "Modeling and nonlinear dynamics of fluid-conveying risers under hybrid excitations," *Int. J. Eng. Sci.*, vol. 81, pp. 1–14, 2014.

[31] Z. Yan, A. Abdelkefi, and M. R. Hajj, "Piezoelectric energy harvesting from hybrid vibrations," *Smart Mater. Struct.*, vol. 23, 2014, Art. 025026.

[32] L. Zhao and Y. Yang, "Enhanced aeroelastic energy harvesting with a beam stiffener," *Smart Mater. Struct.*, vol. 24, 2015, Art. 032001.

[33] D. Guyomar, A. Badel, E. Lefeuvre, and C. Richard, "Toward energy harvesting using active materials and conversion improvement by nonlinear processing," *IEEE Trans. Ultrason., Ferroelect., Freq. Control*, vol. 52, no. 4, pp. 584–595, Apr. 2005.

[34] A. Badel, D. Guyomar, E. Lefeuvre, and C. Richard, "Piezoelectric energy harvesting using a synchronized switch technique," *J. Intell. Mater. Syst. Struct.*, vol. 17, pp. 831–839, 2006.

[35] E. Lefeuvre, A. Badel, C. Richard, and D. Guyomar, "Energy harvesting using piezoelectric materials: Case of random vibrations," *J. Electroceramic*, vol. 19, pp. 349–355, 2007.
[36] Y. C. Shu, I. C. Lien, and W. J. Wu, "An improved analysis of the SSHI interface in piezoelectric energy harvesting," *Smart Mater. Struct.*, vol. 16, pp. 2253–2264, 2007.
[37] I. C. Lien, Y. C. Shu, W. J. Wu, S. M. Shiu, and H. C. Lin, "Revisit of series-SSHI with comparisons to other interfacing circuits in piezoelectric energy harvesting," *Smart Mater. Struct.*, vol. 19, 2010, Art. 125009.
[38] M. Lallart and D. Guyomar, "An optimized self-powered switching circuit for non-linear energy harvesting with low voltage output," *Smart Mater. Struct.*, vol. 17, 2008, Art. no. 035030.
[39] Y. S. Shih, S. C. Lin, M. Lallart, and W. J. Wu, "Self-powered synchronized switching interfacing circuits for micro-piezoelectric energy harvesters," in *Proc. ASME Conf. Smart Mater. Adaptive Struct. Intell. Syst.*, 2013, Art. no. V002T07A005.
[40] W. J. Wu, A. M. Wickenheiser, T. Reissman, and E. Garcia, "Modeling and experimental verification of synchronized discharging techniques for boosting power harvesting from piezoelectric transducers," *Smart Mater. Struct.*, vol. 18, 2009, Art. no. 055012.
[41] A. M. Wickenheiser, T. Reissman, W.-J. Wu, and E. Garcia, "Modeling the effects of electromechanical coupling on energy storage through piezoelectric energy harvesting," *IEEE/ASME Trans. Mechatronics*, vol. 15, no. 3, pp. 400–411, Jun. 2010.
[42] J. Qiu, H. Jiang, H. Ji, and K. Zhu, "Comparison between four piezoelectric energy harvesting circuits," *Frontiers Mech. Eng.*, vol. 4, pp. 153–159, 2009.
[43] H. Ji, J. Qiu, P. Xia, and H. Nie, "Energy conversion and performance of switched-voltage control based on negative capacitance with arbitrary switching frequency," *Smart Mater. Struct.*, vol. 21, 2012, Art. 125010.
[44] J. Liang and W. Liao, "On the influence of transducer internal loss in piezoelectric energy harvesting with SSHI interface," *J. Intell. Mater. Syst. Struct.*, vol. 22, pp. 503–512, 2011.
[45] J. Liang and W.-H. Liao, "Improved design and analysis of self-powered synchronized switch interface circuit for piezoelectric energy harvesting systems," *IEEE Trans. Ind. Electron.*, vol. 59, no. 4, pp. 1950–1960, Apr. 2012.
[46] J. Liang and W.-H. Liao, "Impedance modeling and analysis for piezoelectric energy harvesting systems," *IEEE/ASME Trans. Mechatronics*, vol. 17, no. 6, pp. 1145–1157, Dec. 2012.
[47] L. Zhu, R. Chen, and X. Liu, "Theoretical analyses of the electronic breaker switching method for nonlinear energy harvesting interfaces," *J. Intell. Mater. Syst. Struct.*, vol. 23, pp. 441–451, 2012.
[48] Y. Wu, A. Badel, F. Formosa, W. Liu, and A. Agbossou, "Self-powered optimized synchronous electric charge extraction circuit for piezoelectric energy harvesting," *J. Intell. Mater. Syst. Struct.*, vol. 25, pp. 2165–2176, 2014.
[49] L. Zhao and Y. Yang, "Analytical solutions for galloping-based piezoelectric energy harvesters with various interfacing circuits," *Smart Mater. Struct.*, vol. 24, 2015, Art. 075023.
[50] L. Zhao, L. Tang, and Y. Yang, "Synchronized charge extraction in galloping piezoelectric energy harvesting," *J. Intell. Mater. Syst. Struct.*, vol. 27, pp. 453–468, 2016.
[51] M. Bryant, A. D. Schlichting, and E. Garcia, "Toward efficient aeroelastic energy harvesting: Device performance comparisons and improvements through synchronized switching," *Proc. SPIE*, vol. 8688, 2013, Art. no. 868807.
[52] S. Roundy, P. K. Wright, and J. Rabaey, "A study of low level vibrations as a power source for wireless sensor nodes," *Comput. Commun.*, vol. 26, pp. 1131–1144, 2003.
[53] J. P. Den Hartog, *Mechanical Vibrations*. New York, NY, USA: McGraw-Hill, 1956.
[54] A. Erturk and D. J. Inman, "A distributed parameter electromechanical model for cantilevered piezoelectric energy harvesters," *J. Vib. Acoust. Trans. ASME*, vol. 130, 2008, Art. no. 041002.
[55] J. Liang and W.-H. Liao, "Piezoelectric energy harvesting and dissipation on structural damping," *J. Intell. Mater. Syst. Struct.*, vol. 20, pp. 515–527, 2009.
[56] E. Lefeuvre, A. Badel, C. Richard, L. Petit, and D. Guyomar, "A comparison between several vibration-powered piezoelectric generators for standalone systems," *Sens. Actuat. A Phys.*, vol. 126, pp. 405–416, 2006.
[57] C. Richard, D. Guyomar, and E. Lefeuvre, "Self-powered electronic breaker with automatic switching by detecting maxima or minima of potential difference between its power electrodes," *Patent PCT/FR2005/003000*, Jul. 6, 2007.
[58] L. Tang, L. Zhao, Y. Yang, and E. Lefeuvre, "Equivalent circuit representation and analysis of galloping-based wind energy harvesting," *IEEE/ASME Trans. Mechatronics*, vol. 20, no. 2, pp. 834–844, Apr. 2015.

Liya Zhao was born in Shandong, China, in 1988. She received the B.Eng. degree in civil engineering from Tongji University, Shanghai, China, in 2009, and the Ph.D. degree in structures and mechanics from Nanyang Technological University, Singapore, in 2015.

She is currently a Postdoctoral Research Fellow in the School of Civil and Environmental Engineering, Nanyang Technological University, Singapore. Her main research interests include energy harvesting, smart materials and structures, wind energy, nonlinear dynamics, power electronics, and piezoelectric devices.

Lihua Tang received the B.Eng. degree in engineering mechanics and the M.Eng. degree in solid mechanics from Shanghai Jiao Tong University, Shanghai, China, in 2005 and 2008, respectively, and the Ph.D. degree in structures and mechanics from Nanyang Technological University, Singapore, in 2012.

He has been working as a Lecturer in the Department of Mechanical Engineering, University of Auckland, New Zealand since 2014. His main research interests include smart materials and structures, energy harvesting, nonlinear dynamics, vibration control, metamaterial, and acoustics. He has authored and coauthored more than 50 publications including 30 journal papers.

Dr. Tang is a Member of ASME and SPIE. He is an elected Member of Energy Harvesting Technical Committee of ASME and an elected member of Adaptive Structures and Material Systems (ASMS) Technical Branch of ASME.

Junrui Liang (S'09–M'10) has received the Ph.D. degree in mechanical and automation engineering from the Chinese University of Hong Kong, Hong Kong, in 2010.

He is currently a tenure-track Assistant Professor in the School of Information Science and Technology, ShanghaiTech University, China. He is the author or coauthor of more than 30 technical papers published in international journals and conferences and holds two China patent applications. His research interests include mechatronics, kinetic energy harvesting and vibration control, power electronics, renewable energy, etc.

Dr. Liang was a Program Committee Member of SPIE Smart Structures/NDE conference 2016 and 2017. He is also a Member in the Technical Committee of power and energy circuits and systems in IEEE Circuits and Systems Society since 2016. He received Best Paper Awards at the IEEE International Conference on Information and Automation in 2009 and 2010, and two other research awards. He is a member of ASME.

Yaowen Yang received the B.Eng. degree in engineering mechanics and M.Eng. degree in solid mechanics from Shanghai Jiao Tong University, Shanghai, China, in 1989 and 1992, respectively, and the Ph.D. degree in structures and mechanics from Nanyang Technological University, Singapore, in 2001.

He is currently an Associate Professor at Nanyang Technological University, Singapore. His research interests include smart materials for energy harvesting, structural health monitoring, and vibration control. Over the years, he has published one book, three monographs, and more than 170 journal and conference papers.

Dr. Yang serves as an Editorial Board Member of a number of international journals and as a Member of the ASME Technical Committee on Energy Harvesting.